Strategy to improve the long-term stability of low-stress e-beam coatings

TINGTING ZENG,[1,2] MEIPING ZHU,[1,2,3,6] CHAOYI YIN,[1,2] YUN CUI,[1,2] JIAOLING ZHAO,[1] YANZHI WANG,[1,2] GUOHANG HU,[1,2] YINGJIE CHAI,[4] (iD) AND JIANDA SHAO[1,2,3,5,7]

[1]*Laboratory of Thin Film Optics, Key Laboratory of Materials for High Power Laser, Shanghai Institute of Optics and Fine Mechanics, Shanghai 201800, China*
[2]*Center of Materials Science and Optoelectronics Engineering, University of Chinese Academy of Sciences, Beijing 100049, China*
[3]*Hangzhou Institute for Advanced Study, University of Chinese Academy of Sciences, Hangzhou 310024, China*
[4]*CREOL, The College of Optics and Photonics, University of Central Florida, Orlando, FL 32816, USA*
[5]*CAS Center for Excellence in Ultra-intense Laser Science, Shanghai 201800, China*
[6]*bree@siom.ac.cn*
[7]*jdshao@siom.ac.cn*

Abstract: The performance of the electron-beam (e-beam) coatings can be easily affected by the environmental humidity due to their porous nature. We propose a shell layer strategy deposited by plasma ion-assisted deposition to cover the top surface and sidewall of the e-beam coating. The long-term optical and mechanical stability of the prepared multilayer coatings with and without the shell layer are compared. Our results show that the shell layer strategy can effectively isolate the underlying e-beam coating from the ambient humidity, thereby significantly improving the long-term stability and mechanical properties of the e-beam coating. Meantime, the shell layer strategy of isolating ambient humidity avoids the increase in compressive stress caused by water absorption of the e-beam coating, thereby keeping the entire coating stress at a low level. The proposed shell layer strategy can be used to address the time- and environment-dependent instability issues of the e-beam coatings for high-power laser applications.

1. Introduction

Electron-beam (e-beam) deposited coatings have been widely used in the high-power laser systems worldwide [1–6] due to their relatively high laser-resistance, good spectral uniformity, and the ability to scale to large-aperture [7–16]. The optical and mechanical properties of the e-beam coating can greatly affect the output performance and long-term stability of these high-power laser systems [11,17]. Unfortunately, the porous nature of the e-beam coating allows the absorption and desorption of water, making the coating susceptible to environmental conditions, especially environmental humidity [18–20]. Changes in the environment (for example, from the atmosphere to a vacuum environment) can cause spectral shifts, resulting in changes in the transmittance/reflectance and the laser-induced damage threshold (caused by changes in the e-field distribution) at the laser wavelength [21–23]. All the unsteadiness would in turn cause the instability of output laser power. The environmental transition can also cause changes in coating stress and may induce coating cracking [24,25]. Even in a controlled environment, the performance of the e-beam coating can change with increasing aging time [21,26,27]. Time- or environment-related stress evolution, whether it is compressive or tensile, can deform the coating surface and change the wave-front, thereby affecting the beam transmission and focusing [10,11,17,19,28].

A lot of work has studied the influence of environmental humidity on the optical and mechanical properties of e-beam coatings [19,24,26,29,30]. A deep understanding of the stress evolution of e-beam coatings during coating deposition and vacuum-air exposure process was enabled thanks to the potential offered by the in-situ stress monitoring system [31–33]. A dense capping layer method was proposed to prolong the originally rapid water absorption process of the e-beam coating, thus enabling the study of water vapor transmission rate and the performance instability of the e-beam coating caused by moisture [29]. Many strategies have been proposed to obtain coatings with low stress in a controlled environment, including thermal oxide patterning based correction, optimizing the deposition parameters to minimize the stress of different materials, and optimizing the coating design to balance the opposite stresses between high- and low- refractive index materials, as well as applying an under-layer with opposite stress or applying the same coating on the backside of the substrate to minimize the wave-front change of the coated optics [24,34–38]. Among the above strategies, only the strategy of applying the same coating on the backside can reduce the wave-front change caused by the coating, while avoiding the wave-front change caused by environmental change or aging effect. However, this method may cause unwanted reflection on the back of the optics, which limits the applicability of this method. How to obtain low-stress e-beam coatings with long-term stability has not been addressed.

To achieve the low-stress e-beam coatings with long-term stability, first, the radial water vapor diffusion from the sidewall to the center of the e-beam coating is experimentally verified by using a plasma ion-assisted deposition (PIAD) SiO_2 capping layer (covering the top surface only). Then, a PIAD SiO_2 shell layer covering both the top surface and the sidewall of the e-beam coating is proposed and experimentally demonstrated to isolate the inner e-beam coating from environmental humidity completely. The long-term optical and mechanical stability of the prepared multilayer coatings with and without a PIAD SiO_2 shell layer has been comparatively studied. The multilayer coating with a PIAD SiO_2 shell layer shows improved long-term stability over traditional e-beam multilayer coating. The proposed shell layer strategy provides a new way to prepare a low-stress e-beam coating with significantly improved long-term stability.

2.   Material and methods

2.1.   Sample fabrication

A PIAD monolayer S1 (substrate|4C|air), two bilayer coatings B1 (substrate|3.35H1.65C|air) and B2 (substrate|5.42L1.65C|air), and three multilayer coatings including traditional multilayer (TM), multilayer with a capping layer (MCL), multilayer with a shell layer (MSL), are deposited by an evaporation coater with plasma assist system. The deposition technology has the advantage of excellent uniformity. BK7, ZF7 and BaF_2 substrates are used for stress, UV/VIS/NIR spectrum and Fourier transform infrared (FTIR) characterization, respectively. As shown in Fig. 1, coating TM with the structure of substrate|4L(HL)^{12}H4L|air is prepared in one coating run, while coatings MCL and MSL with the structure of substrate|4L(HL)^{12}H4C4C|air are prepared in two coating runs. In run 1, substrate holders which cover the substrate edge about 3 mm are used, and the underlying layers 4L(HL)^{12}H4C are deposited. In run 2, half of the samples that prepared in run 1 are moved to substrate holders which cover the substrate edge about 1 mm, and then the top 4C layer is deposited onto the underlying layers and the newly exposed bare substrate area, serving as a shell layer. For the uniformity of the shell layer, the influence of the shadow effect caused by the underlying layers should be considered. In this work, the shell layer in coating MSL covers both the top surface and sidewall of the underlying layers with good uniformity because the thickness of the underlying layers is only about several microns, which does not degrade the uniformity of the coating. The other half of the samples stick to the previous substrate holder, and the top 4C layer is deposited onto the top surface of the underlying layers only, serving as a capping layer of coating MCL. Between the run 1 and run 2, the coatings are exposed to the atmosphere as short as possible to reduce the amount of water adsorbed through the coating sidewall. Here,

H, L and C denote HfO_2, SiO_2 and PIAD SiO_2 layer with a quarter-wave optical thickness at a reference wavelength of 1064 nm, respectively. H and L layers are deposited by conventional e-beam evaporation with Hf and SiO_2 as starting materials, while C layer is deposited by PIAD at a bias of 170V. The coating chamber is evacuated to a base pressure of 9×10^{-4} Pa, and the substrates are baked to 200 °C before deposition. H, L and C layers are deposited at a rate of ~0.14 nm/s, 0.6 nm/s and 0.4 nm/s, respectively. The oxygen pressures for H and L layers are 1.4 $\times 10^{-2}$ Pa and 5.5×10^{-3} Pa, respectively. An Ar/O_2 mixture at a pressure of about 3×10^{-2} Pa is used for C layers.
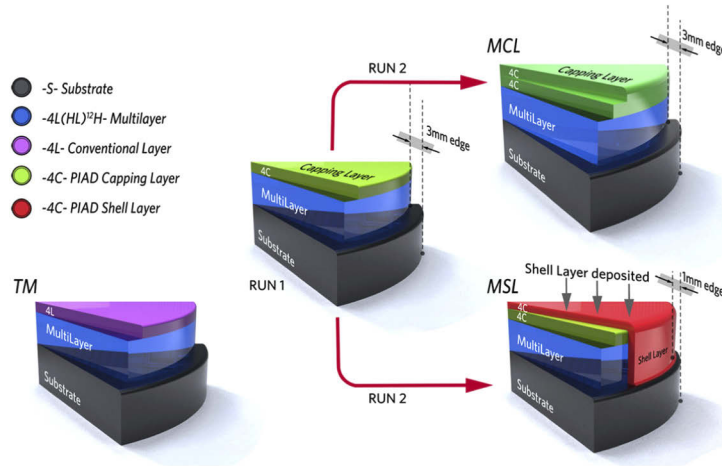

Fig. 1. Schematic diagram of multilayer coatings TM, MCL and MSL.

2.2. Sample characterization

Samples are stored and characterized in a Class 1000 clean room with a controlled temperature of 23 ± 1.5 °C and relative humidity of $45 \pm 5\%$. The chemical composition is determined by an X-ray photoelectron spectroscopy (XPS, Thermo Scientific K-Alpha) equipped with a monochromatic Al Kα X-ray source. The spectra are recorded after 20 s of etching with 1 KeV Ar^+ ions. The UV/VIS/NIR transmission spectra are measured by a spectrometer (Lambda 1050 UV/VIS/NIR, Perkin-Elmer). The water absorption phenomenon is confirmed by a Fourier transform infrared spectrometer (FTIR; Bruker, VERTEX 70) in transmittance mode from 4000 cm^{-1} to 400 cm^{-1} at a 4 cm^{-1} resolution. The moisture isolation effect of the shell layer on the e-beam coating is investigated by the water bath treatment in a water bath cabinet. The surface and cross-section morphologies of coating before and after the water bath treatment are characterized by an optical microscope (BX53M Olympus) and a focused ion beam-scanning electron microscope (FIB-SEM, Carl Zeiss AURIGA CrossBeam). Prior to the FIB-SEM characterization, the samples are coated with a thin layer of Cr to prevent surface charging. The anti-scratch property is tested with a nanoindenter (KLA Tencor G200). The diamond stylus moves over the specimen surface with constant normal force load (0.5, 1.0, 3.0 mN, respectively) at a scratching rate of 30 μm/s. The scratching length is 300 μm. Scratch morphologies are characterized by the optical microscope. The sample surface before (substrate) and every several days after deposition is characterized by an optical interferometer (ZYGO Mark III-GPI).

3. Results and discussion

3.1. Moisture-proof property of PIAD SiO_2 layer

To verify that the PIAD SiO_2 layer in this work is moisture-proof, XPS characterization is performed on the top layers of the multilayer coating TM and MSL which have experienced an

aging time of 3 years. As shown in Fig. 2, the O 1s spectrum of the top 4L layer of TM can be fitted into two Lorentzian-Gaussian peaks centered at 532.98 eV (Si−O) and 531.67 eV (-OH), respectively [39]. However, the O 1s spectrum of the shell layer of MSL can be well fitted into a Lorentzian-Gaussian peak centered at 532.92 eV (Si−O), no water absorption induced peak (-OH) is observed [40]. The XPS analysis indicates that the PIAD SiO_2 layer is water-free even after long-term aging and can serve as a moisture-proof layer.
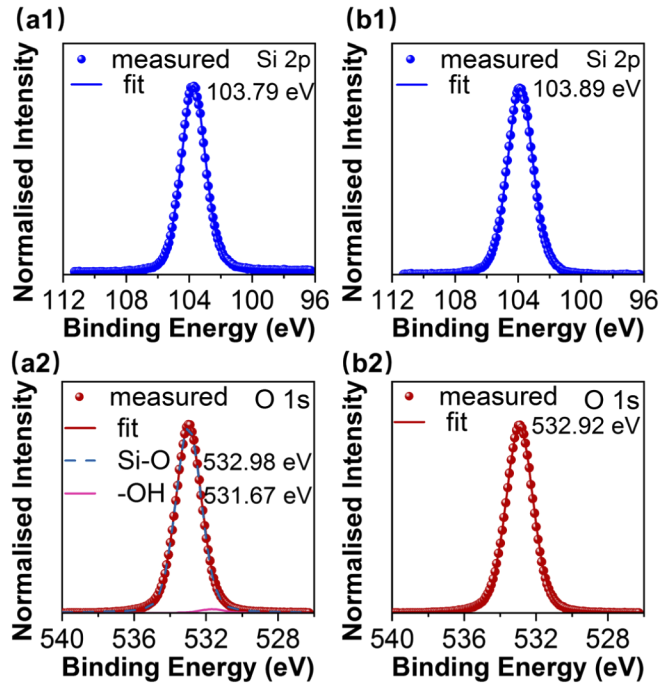

Fig. 2. (a1), (a2) XPS spectra of Si 2p and O 1s core level for the top 4L layer of coating TM. (b1), (b2) XPS spectra of Si 2p and O 1s core level for the shell layer of MSL.

3.2. Radial water vapor diffusion

In order to study the radial water vapor diffusion, the UV/VIS/NIR spectral uniformity along the radius of the bilayer coating B1 is tested within a few days after coating. Three spots A, B and C evenly distributed from the coating center to the edge at an interval of 6 mm are tested. The diameter of the test spot is 2 mm. As illustrated in Fig. 3(a1-a3), the spectra measured at the three spots coincide on day 1, and the spectral redshift is first observed in the spectrum of spot C, then followed by spot B and spot A, indicating that there is a concentration gradient of water molecules along the radius of the bilayer coating system.

The center of coatings TM, B1, and B2 are characterized by FTIR. On day 1, an intensive water absorption peak in the range of 2700-3800 cm^{-1} is observed in the FTIR spectrum of coating TM, the water absorption peak does not change much after aging for about 170 days, as shown in Fig. 3(b1). The reason is that for the coating TM, water can be transported through both the top surface and the sidewall, and the absorption of water is almost "instantaneous" during the exposure of the coating from the vacuum chamber to the atmospheric environment. As shown in Fig. 3(b2, b3), no water absorption peak is observed in the FTIR spectra of the coatings B1 and B2 with a capping layer on day 2, while a clear water absorption peak is observed after an aging time of about 170 days. The UV/VIS/NIR transmission and FTIR measurement results
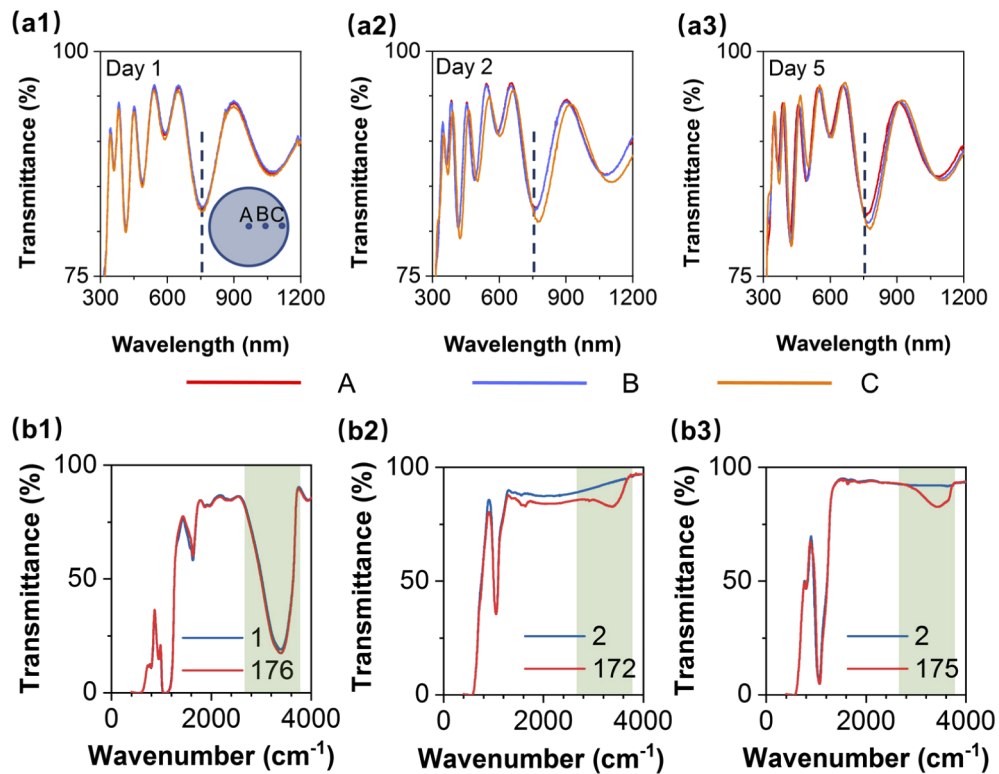
Fig. 3. (a1), (a2), and (a3) Transmission spectra of the three spots of bilayer coating B1 measured on day 1, day 2 and day 5, respectively. The inset is the schematic diagram of the spectral measurement along the coating radius. (b1), (b2) and (b3) FTIR transmission spectra of coatings TM, B1, and B2 versus aging time, respectively.

confirm that for coatings with a capping layer, water can be transported through the sidewall of the coating. A capping layer strategy that only seals the top surface is insufficient to achieve an e-beam coating with long-term stability.

3.3. Moisture isolation effect verification of the shell layer

In order to completely separate the porous e-beam coating from environmental humidity, a shell layer strategy covering both the top surface and sidewall of e-beam coating is proposed, and a water bath treatment is employed to remove the top PIAD SiO_2 layer of the coating MSL to verify the moisture isolation effect of the shell layer. Coatings TM and MSL are immersed in deionized water at 90 °C for 24 hours, as illustrated in Fig. 4(a). Figure 4(b1) shows that the shell layer of coating MSL is continuous and smooth between the top surface and the sidewall before the water bath treatment. It indicated that the dense shell layer can encapsulate the inner e-beam coating with good continuity to ensure adequate moisture isolation effect. After the water bath treatment, the PIAD SiO_2 layer of coating MSL is peeled off from the underlying e-beam layers as expected, but the part on the substrate remains coated onto the substrate with excellent adhesion, see Fig. 4(b2, b3). The peeling phenomenon can be attributed to the poor adhesion induced by the mismatch between the large compressive stress (−424.4 MPa) of the PIAD SiO_2 layer and the tensile stress of the underlying e-beam coating. In comparison, the coating TM suffers severe water corrosion, and blisters appear on the surface and edge of the coating. The

FIB characterization results indicate that the blisters are originated from nodular defects with water diffusion channels at the boundary, see Fig. 4(c1, c2).
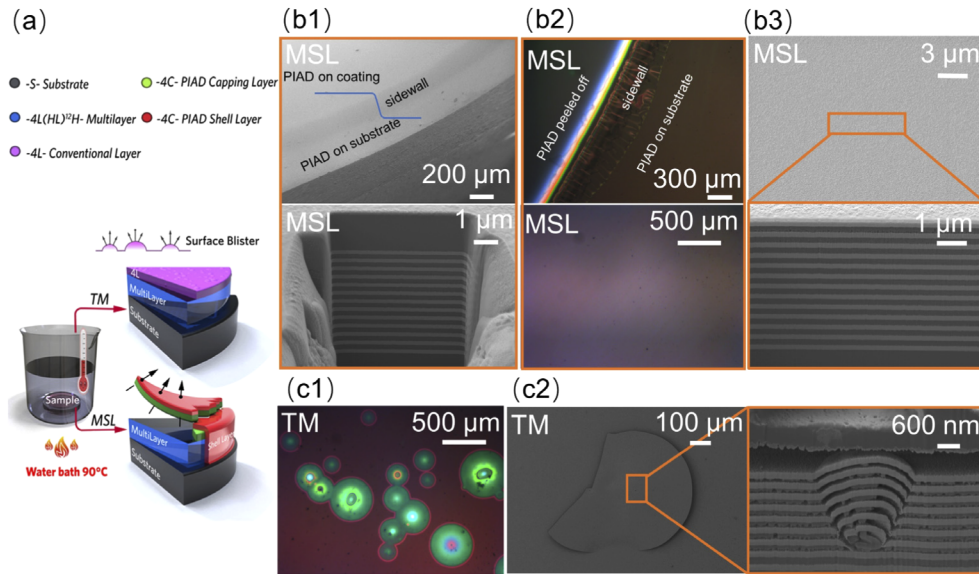

Fig. 4. (a) Schematic diagram of multilayer coatings TM and MSL after water bath treatment. (b1) SEM morphologies of the surface edge (up) and cross-sectional morphology (down) of coating MSL before water bath treatment. (b2) Optical microscope morphologies of the surface edge (up) and the top surface (down) of coating MSL after water bath treatment. (b3) SEM surface (up) and cross-sectional (down) morphologies of coating MSL after water bath treatment. (c1, c2) Optical microscope morphology and SEM surface and cross-sectional morphologies of coating TM after water bath treatment, respectively.

The spectra of coatings TM and MSL before and after water bath treatment are compared in Fig. 5. No wavelength shift but a decrease of the overall transmittance in the spectrum of the coating TM is observed after water bath treatment. The decrease in transmittance can be attributed to the increased scattering caused by the high-density blisters on the surface of the coating after water bath treatment. A clear spectral redshift is observed in the spectrum of the
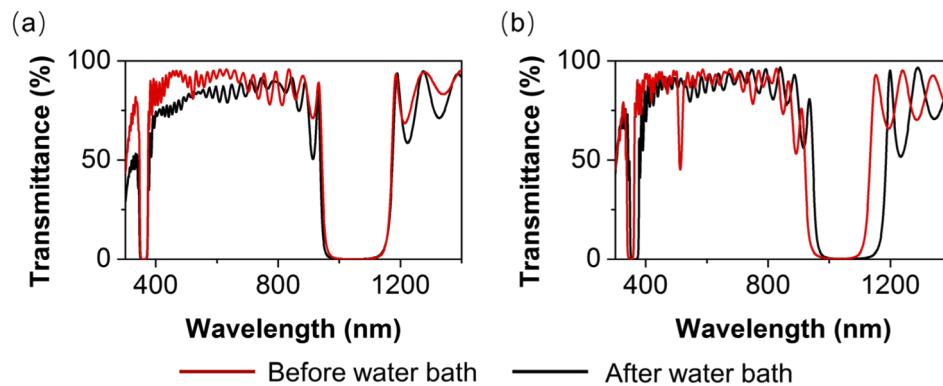

Fig. 5. (a), (b) Transmission spectra before and after water bath treatment of coatings TM and MSL, respectively.

coating MSL after water bath treatment. The underlying porous e-beam coating absorbs a lot of water after the top PIAD SiO$_2$ layer is peeled off. The difference in the spectra ripple near the 500 nm before and after water bath treatment can be explained as follows: For the design of coating MSL, the refractive index and extinction coefficient of H and L layer are the same as that of coating TM. The designed optical thickness ratio of H to L is 1:1 in the atmosphere. However, the actual optical thickness ratio of H to L derives from 1:1 because the H and L layer in MSL do not absorb water. The mismatch of the optical thickness of H and L layer results in the observed ripple near the 500 nm. After the shell layer is peeled off in the water bath treatment, the optical thickness of H and L is identical with the design value due to the adsorption of water, and therefore the ripple near the 500 nm disappears. The results of the water bath treatment demonstrate that the PIAD shell layer can effectively isolate the porous e-beam coating from the ambient humidity.

3.4. Mechanical performance and long-term stability

3.4.1. Scratch resistance

To investigate the mechanical property, the scratch test is conducted on the multilayer coatings TM and MSL. Figure 6(a) shows the optical microscope morphologies of different scratches. The applied constant normal forces are 0.5 mN, 1.0 mN and 3.0 mN, respectively. Under the same magnification, the 1.0 mN and 3.0 mN induced scratches can be observed on the coating TM while only the 3.0 mN induced scratch can be observed on the coating MSL. Figure 6(b) shows the depth profiles of the scratch grooves. Compared with coating TM, coating MSL shows a smaller groove depth when subjected to the same normal force. It means that the coating MSL exhibits an enhanced scratch resistance.
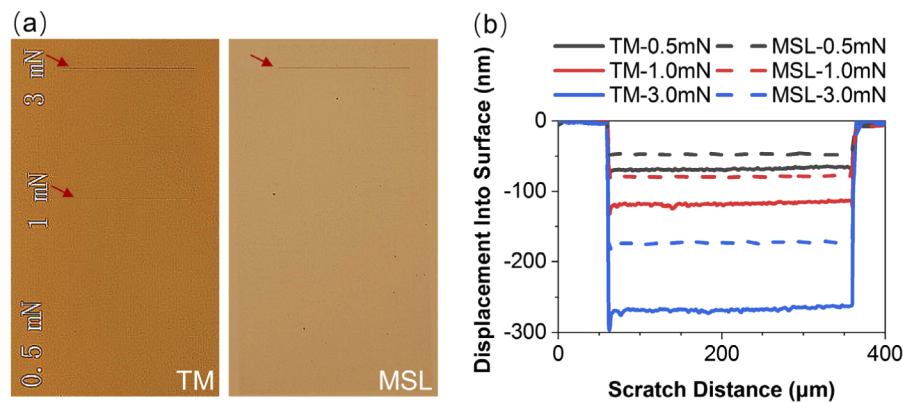

Fig. 6. (a) Optical microscope morphologies of different scratches on coatings TM and MSL. (b) Depth profiles along the center of scratch grooves on coatings TM and MSL.

3.4.2. Long-term stability of spectral and stress properties

The transmission spectra of the multilayer coatings MCL and MSL are regularly measured to investigate the long-term spectral stability. The wavelength (λ_p) at peak reflectivity versus aging time is shown in Fig. 7(a). The multilayer coating MCL with a capping layer experiences a large spectral redshift, and it takes about 90 days to reach a relatively stable spectrum since water can only be transported through the sidewall. At the steady state after 90 days of aging, the spectral fluctuations of the coating MCL can be attributed to the swelling and refilling effect caused by the large amount of water infiltration [29]. The spectrum of the coating MSL stabilizes in a short time, and the amount of spectral redshift is relatively small because the shell layer isolates the

porous e-beam coating from the ambient humidity. Compared with the coating MCL, the coating MSL shows a more stable spectrum under the steady state due to less absorbed water.
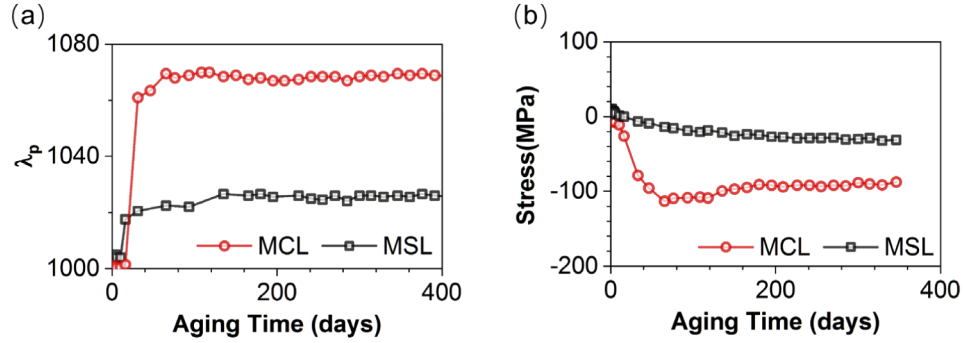

Fig. 7. (a) Wavelengths at peak reflectivity of coatings MCL and MSL versus aging time. (b) Stresses of coatings MCL and MSL versus aging time.

The stress evolution curves of coatings MCL and MSL versus aging time is shown in Fig. 7(b). On day 1, the stresses of the coatings MCL and MSL are very close. Due to the water transport from the sidewall, the stress of the coating MCL gradually changes from 9.5 MPa to −113.3 MPa. Then, the compressive stress relaxes gradually during the aging process. The stress of coating MSL varies slightly and stabilizes at low compressive stress. The shell layer of the coating MSL can effectively improve the long-term stress stability of the e-beam coating by preventing water molecules from being incorporated into the porous e-beam coating. Meanwhile, preventing the incorporation of water also helps to reduce the high compressive stress induced by the large amount of water absorption [19], which makes it possible to keep the entire coating stress at a low compressive level. The small spectral shift and slight stress evolution exhibited by the coating MSL are attributed to the diffusion of water that penetrated through the sidewall of the coating during the exposure process between the two coating runs.

3.4.3. Stress component analysis

The shell layer prevents water from penetrating the inner e-beam layers, so that the stress of the layers without water absorption can be calculated. The measured stress σ of the coating TM consists of intrinsic stress σ_i and water-related stress σ_w, which arises from coating structure, and interaction between water molecules and coating pores, respectively.

$$\sigma = \sigma_i + \sigma_w, \tag{1}$$

The measured stress σ_υ of the coating MSL and unaged coatings B1, B2 and MCL can be regarded as the stress without water since only a small amount of water is absorbed.

$$\sigma_\upsilon = \sigma_i = \frac{\sigma_{\upsilon-H}T_H + \sigma_{\upsilon-L}T_L + \sigma_{\upsilon-C}T_C}{T_{total}} + (n-1)\sigma_{\upsilon-\text{int}}, \tag{2}$$

Where, $\sigma_{\upsilon-H}$, $\sigma_{\upsilon-L}$, $\sigma_{\upsilon-C}$ and $\sigma_{\upsilon-\text{int}}$ are the stresses of H, L, C layers and interface without water, respectively. T_H, T_L, T_C and T_{total} are the total physical thicknesses of H, L, C layers and entire coating, respectively. n is the number of layers, (n-1) is the number of layer interfaces. The four stresses included in Eq. (2) can be solved by establishing a linear sequence of four equations [24]. In this work, the data of four coatings are used for calculations. The detailed information is listed in Table 1.

Table 1. Sample information for stress component analysis

Sample	T_H (nm)	T_L (nm)	T_C (nm)	T_{total} (nm)	n-1	σ_υ (MPa)
S1	0	0	705	705	0	−424.4
B1	500	0	291	791	1	76.1
B2	0	1000	291	1291	1	−101.0
MSL	1940	2952	1410	6302	26	10.3

For the given coatings, the calculation is constructed in matrix form:

$$
\begin{bmatrix}
\frac{T_{H-S1}}{T_{total-S1}} & \frac{T_{L-S1}}{T_{total-S1}} & \frac{T_{C-S1}}{T_{total-S1}} & (n-1)_{S1} \\
\frac{T_{H-B1}}{T_{total-B1}} & \frac{T_{L-B1}}{T_{total-B1}} & \frac{T_{C-B1}}{T_{total-B1}} & (n-1)_{B1} \\
\frac{T_{H-B2}}{T_{total-B2}} & \frac{T_{L-B2}}{T_{total-B2}} & \frac{T_{C-B2}}{T_{total-B2}} & (n-1)_{B2} \\
\frac{T_{H-MSL}}{T_{total-MSL}} & \frac{T_{L-MSL}}{T_{total-MSL}} & \frac{T_{C-MSL}}{T_{total-MSL}} & (n-1)_{MSL}
\end{bmatrix}
\times
\begin{bmatrix}
\sigma_{\upsilon-H} \\
\sigma_{\upsilon-L} \\
\sigma_{\upsilon-C} \\
\sigma_{\upsilon-int}
\end{bmatrix}
=
\begin{bmatrix}
\sigma_{\upsilon-S1} \\
\sigma_{\upsilon-B1} \\
\sigma_{\upsilon-B2} \\
\sigma_{\upsilon-MSL}
\end{bmatrix},
\qquad (3)
$$

Solving Eq. (3) with the input parameters listed in Table 1. The solutions are summarized in Table 2.

Table 2. Solutions to the system of equations describing the individual stress contributions.

Component	$\sigma_{\upsilon-H}$	$\sigma_{\upsilon-L}$	$\sigma_{\upsilon-C}$	$\sigma_{\upsilon-int}$
Value (MPa)	367.7	−6.7	−424.4	−0.2

To verify the correctness, we use the above-calculated stress values to predict the total stress of a multilayer coating which with a design structure of substrate|4L(HL)^{12}H4C|air. The coating stress without water absorption is predicted to be 65.3 MPa, and the measured stress of the as-deposited coating is 66.9 MPa. The predicted value consistent with the experimental result well.

4. Conclusion

In summary, we have proposed and experimentally demonstrated a shell layer strategy for preparing low-stress e-beam coatings with enhanced long-term stability. The proposed shell layer strategy covers both the top surface and sidewall of the porous e-beam coatings with a dense PIAD layer, it can effectively isolate the inner e-beam coating from environmental humidity. The experimental results demonstrate that the shell layer strategy has several advantages. First, it avoids the increase in compressive stress caused by water absorption of the e-beam coating, thereby achieving a low-stress coating. Second, it improves the long-term stability of the spectrum and stress of the coating. Third, it enhances the anti-scratch property of the coating. Fourth, it enables to evaluate the stress of the coating without water in an atmospheric environment, which is traditionally obtained by performing wave-front measurements in a vacuum environment. We believe that the proposed strategy opens a new pathway for low-stress e-beam coatings with enhanced long-term stability.

Disclosures

The authors declare no conflicts of interest.

References

1. C. Macilwain, "Inadequate optics "threat to US laser facility," Nature **403**(6766), 120 (2000).
2. "Extreme light," Nat. Mater. **15**(1), 1 (2016).
3. F. Wang, S. Jiang, Y. Ding, S. Liu, J. Yang, S. Li, T. Huang, Z. Cao, Z. Yang, X. Hu, W. Miao, J. Zhang, Z. Wang, G. Yang, R. Yi, Q. Tang, L. Kuang, Z. Li, D. Yang, Y. Li, X. Peng, K. Ren, and B. Zhang, "Recent diagnostic developments at the 100 kJ-level laser facility in China," Matter Radiat. Extremes **5**(3), 035201 (2020).
4. Z. Zhang, F. Wu, J. Hu, X. Yang, J. Gui, P. Ji, X. Liu, C. Wang, Y. Liu, X. Lu, Y. Xu, Y. Leng, R. Li, and Z. Xu, "The 1 PW/0.1 Hz laser beamline in SULF facility," High Power Laser Sci. Eng. **8**, e4–7 (2020).
5. D. Besnard, "The megajoule laser program – ignition at hand," Eur. Phys. J. D **44**(2), 207–213 (2007).
6. C. Danson, D. Hillier, N. Hopps, and D. Neely, "Petawatt class lasers worldwide," High Power Laser Sci. Eng. **3**, e3–14 (2015).
7. X. Cheng, J. Zhang, T. Ding, Z. Wei, H. Li, and Z. Wang, "The effect of an electric field on the thermomechanical damage of nodular defects in dielectric multilayer coatings irradiated by nanosecond laser pulses," Light: Sci. Appl. **2**(6), e80 (2013).
8. T. Tolenis, L. Grinevičiute, L. Smalakys, M. Ščiuka, R. Drazdys, L. Mažule, R. Buzelis, and A. Melninkaitis, "Next generation highly resistant mirrors featuring all-silica layers," Sci. Rep. **7**(1), 10898 (2017).
9. Y. Chai, M. Zhu, Z. Bai, K. Yi, H. Wang, Y. Cui, and J. Shao, "Impact of substrate pits on laser-induced damage performance of 1064-nm high-reflective coatings," Opt. Lett. **40**(7), 1330–1333 (2015).
10. H. Qi, M. Zhu, M. Fang, S. Shao, C. Wei, K. Yi, and J. Shao, "Development of high-power laser coatings," High Power Laser Sci. Eng. **1**(1), 36–43 (2013).
11. J. H. Campbell, R. A. Hawley-Fedder, C. J. Stolz, J. A. Menapace, M. R. Borden, P. K. Whitman, J. Yu, M. J. Runkel, M. O. Riley, M. D. Feit, and R. P. Hackel, "NIF optical materials and fabrication technologies: an overview," Proc. SPIE **5341**, 84–101 (2004).
12. H. Jiao, T. Ding, and Q. Zhang, "Comparative study of Laser induce damage of HfO₂/SiO₂ and TiO₂/SiO₂ mirrors at 1064 nm," Opt. Express **19**(5), 4059–4066 (2011).
13. J. B. Oliver, T. J. Kessler, C. Smith, B. Taylor, V. Gruschow, J. Hettrick, and B. Charles, "Electron-beam–deposited distributed polarization rotator for high-power laser applications," Opt. Express **22**(20), 23883 (2014).
14. J. B. Oliver, C. Smith, J. Spaulding, A. L. Rigatti, B. Charles, S. Papernov, B. Taylor, J. Foster, C. W. Carr, R. Luthi, B. Hollingsworth, and D. Cross, "Glancing-angle–deposited magnesium oxide films for high-fluence applications," Opt. Mater. Express **6**(7), 2291 (2016).
15. T. Tolenis, L. Grinevičiūtė, R. Buzelis, L. Smalakys, E. Pupka, S. Melnikas, A. Selskis, R. Drazdys, and A. Melninkaitis, "Sculptured anti-reflection coatings for high power lasers," Opt. Mater. Express **7**(4), 1249 (2017).
16. M. Zhu, N. Xu, B. Roshanzadeh, S. T. P. Boyd, W. Rudolph, Y. Chai, and J. Shao, "Nanolaminate-based design for UV laser mirror coatings," Light: Sci. Appl. **9**(1), 20 (2020).
17. C. J. Stolz, M. J. Runkel, M. S. McBurney, R. E. Cheek, and J. A. Menapace, "Metrology of mirrors for the National Ignition Facility," Proc. SPIE **5341**, 114–120 (2004).
18. H. A. Macleod, "Microstructure of optical thin films," Proc. SPIE **0325**, 21–28 (1982).
19. H. Leplan, B. Geenen, J. Y. Robic, and Y. Pauleau, "Residual stresses in evaporated silicon dioxide thin films: Correlation with deposition parameters and aging behavior," J. Appl. Phys. **78**(2), 962–968 (1995).
20. X. Cheng, S. Dong, S. Zhi, S. Paschel, I. Balasa, D. Ristau, and Z. Wang, "Waterproof coatings for high-power laser cavities," Light: Sci. Appl. **8**(1), 12 (2019).
21. C. J. Stolz, J. R. Taylor, W. K. Eickelberg, and J. D. Lindh, "Effects of vacuum exposure on stress and spectral shift of high reflective coatings," Appl. Opt. **32**(28), 5666 (1993).
22. W. H. Lowdermilk, D. Milam, and F. Rainer, "Optical coatings for laser fusion applications," Thin Solid Films **73**(1), 155–166 (1980).
23. W. Riede, P. Allenspacher, L. Jensen, and M. Jupé, "Analysis of the air-vacuum effect in dielectric coatings," Proc. SPIE **7132**, 71320F (2008).
24. J. B. Oliver, P. Kupinski, A. L. Rigatti, A. W. Schmid, J. C. Lambropoulos, S. Papernov, A. Kozlov, C. Smith, and R. D. Hand, "Stress compensation in hafnia/silica optical coatings by inclusion of alumina layers," Opt. Express **20**(15), 16596 (2012).
25. E. V. Etzkorn and D. R. Clarke, "Cracking of GaN films," J. Appl. Phys. **89**(2), 1025–1034 (2001).
26. J. F. Anzellotti, D. J. Smith, R. J. Sczupak, and Z. Roman Chrzan, "Stress and environmental shift characteristics of HfO₂/SiO₂ multilayer coatings," Proc. SPIE **2966**, 258–264 (1997).
27. O. Stenzel, S. Wilbrandt, N. Kaiser, M. Vinnichenko, F. Munnik, A. Kolitsch, A. Chuvilin, U. Kaiser, J. Ebert, S. Jakobs, A. Kaless, S. Wüthrich, O. Treichel, B. Wunderlich, M. Bitzer, and M. Grössl, "The correlation between mechanical stress, thermal shift and refractive index in HfO₂, Nb₂O₅, Ta₂O₅ and SiO₂ layers and its relation to the layer porosity," Thin Solid Films **517**(21), 6058–6068 (2009).
28. R. A. Zacharias, E. S. Bliss, S. Winters, R. A. Sacks, M. Feldman, A. Grey, J. A. Koch, C. J. Stolz, J. S. Toeppen, L. Van Atta, and B. W. Woods, "Wavefront control of high-power laser beams in the National Ignition Facility (NIF)," Proc. SPIE **3889**, 332–343 (2000).

29. T. Zeng, M. Zhu, Y. Chai, C. Yin, N. Xu, K. Yi, Y. Wang, Y. Zhao, G. Hu, and J. Shao, "Effects of water adsorption on properties of electron-beam HfO$_2$/SiO$_2$ high-reflection coatings," Thin Solid Films **697**, 137826 (2020).

30. S. Jena, R. B. Tokas, S. Thakur, and D. V. Udupa, "Study of aging effects on optical properties and residual stress of HfO$_2$ thin film," Optik **185**, 71–81 (2019).

31. K. Kusaka, T. Hanabusa, M. Nishida, and F. Inoko, "Residual stress and in-situ thermal stress measurement of aluminum film deposited on silicon wafer," Thin Solid Films **290-291**, 248–253 (1996).

32. M. Fang, D. Hu, and J. Shao, "Evolution of stress in evaporated silicon dioxide thin films," Chin. Opt. Lett. **8**(1), 119–122 (2010).

33. J. Li, M. Fang, H. He, J. Shao, Z. Fan, and Z. Li, "Growth stress evolution in HfO$_2$/SiO$_2$ multilayers," Thin Solid Films **526**, 70–73 (2012).

34. Y. Yao, B. D. Chalifoux, R. K. Heilmann, and M. L. Schattenburg, "Thermal oxide patterning method for compensating coating stress in silicon substrates," Opt. Express **27**(2), 1010 (2019).

35. H. Liu, L. Jensen, P. Ma, and D. Ristau, "Stress compensated anti-reflection coating for high power laser deposited with IBS SiO$_2$ and ALD Al$_2$O$_3$," Appl. Surf. Sci. **476**, 521–527 (2019).

36. Y. Yao, X. Wang, J. Cao, M. E. Graham, S. Vaynman, S. E. Grogans, Y. Cao, and M. P. Ulmer, "Stress manipulated coating for figure reshape of light weight X-ray telescope mirrors," Proc. SPIE **9603**, 96031J (2015).

37. A.-C. Probst, T. Begou, T. Döhring, S. Zeising, M. Stollenwerk, J. Stadtmüller, F. Emmerich, and J. Lumeau, "Coating stress analysis and compensation for iridium-based x-ray mirrors," Appl. Opt. **57**(29), 8775 (2018).

38. B. D. Chalifoux, Y. Yao, H. E. Zuo, R. K. Heilmann, and M. L. Schattenburg, "Compensating film stress in silicon substrates for the Lynx X-ray telescope mission concept using ion implantation," Proc. SPIE **10699**, 1069959 (2018).

39. A. C. Bronneberg, C. Höhn, and R. Van De Krol, "Probing the Interfacial Chemistry of Ultrathin ALD-Grown TiO$_2$ Films: An In-Line XPS Study," J. Phys. Chem. C **121**(10), 5531–5538 (2017).

40. E. Chason, "A kinetic analysis of residual stress evolution in polycrystalline thin films," Thin Solid Films **526**, 1–14 (2012).